Chapter 3

Transmission Electron Microscopy

When electrons are accelerated up to high energy levels (few hundreds keV) and focused on a material, they can scatter or backscatter elastically or inelastically, or produce many interactions, source of different signals such as X-rays, Auger electrons or light (Fig. 3.1). Some of them are used in transmission electron microscopy (TEM).

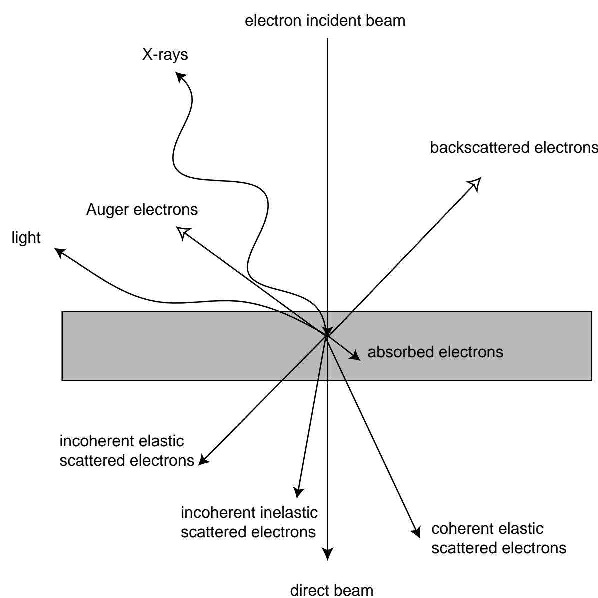

Fig. 3.1 Interactions between electrons and material

The purpose of this chapter is to introduce TEM and the different related techniques used for the microstructural study of the AMCs. The TEM sample preparation of AMCs is described in chapter 3.2. The chemical analyses by energy dispersive spectrometry (EDS) is presented in chapter 3.3. Chapter 3.4 is concerned with the theoretical basis of TEM (diffusion and diffraction). Chapter 3.5 deals with the contrast image formation in a conventional TEM (bright/dark field modes, and diffraction patterns). A brief presentation of high resolution transmission electron microscopy (HREM) with an introduction to electron crystallography is given in chapters 3.6 and 3.7.

3.1 Historical Introduction

The *resolution* ρ of a microscope is defined as the distance between two details just separable from one another. It can be calculated using the Abb theory of images formation for optic systems. For incoherent light or electron beam:

$$\rho = \frac{0.61\lambda}{\sin\alpha} \quad \text{(Rayleigh criterion)} \qquad (3.1)$$

where λ is the wavelength of the light, and α the maximum angle between incident and deflected beam in the limit of the lens aberrations.

For optical microscopy, the resolution is therefore limited by the wavelength of light (410-660 nm). The X or γ rays have lower wavelength, but unfortunately, high-performance lenses necessary to focus the beam to form an image do not exist yet (however, X-rays can reveal structural information of materials by diffraction techniques). In 1923, De Broglie showed that all particles have an associated wavelength linked to their momentum: $\lambda = h/mv$ where m and v are the relativist mass and velocity respectively, and h the Plank's constant. In 1927, Hans Bush showed that a magnetic coil can focus an electron beam in the same way that a glass lens for light. Five years later, a first image with a TEM was obtained by Ernst Ruska and Max Knoll [42]. In a TEM, the electrons are accelerated at high voltage (100-1000 kV) to a velocity approaching the speed of light (0.6-0.9 c); they must therefore be considered as relativistic particles. The associated wavelength is five orders of magnitude smaller than the light wavelength (0.04-0.008 Å). Nevertheless, the magnetic lens aberrations limit the convergence angle of the electron beam to 0.5° (instead of 70° for the glass lens used in optics), and reduce the TEM resolution to the Å order. This resolution enables material imaging (section 3.5) and structure determination at the atomic level (section 3.6 and 3.7). In the 1950s, Raymond Castaing developed an electron probe and X-ray detector for the chemical analyses. A modified version of his technique, the energy dispersive spectrometry EDS (section 3.3) is nowadays usually added to the TEM. Many different techniques based on TEM are used in materials science. Some of them will be detailed in the following sections.

3.2 Preparation of the TEM Samples

For TEM observations, thin samples are required due to the important absorption of the electrons in the material. High acceleration voltage reduces the absorption effects but can cause radiation damage (estimated at 170 kV for Al). At these acceleration tensions, a maximum thickness of 60 nm is required for TEM and HREM observations and quantifications. For Al alloys, this thickness can be obtained by electropolishing with a solution of 20% nitric acid and 80% methanol, but this method is not convenient for the

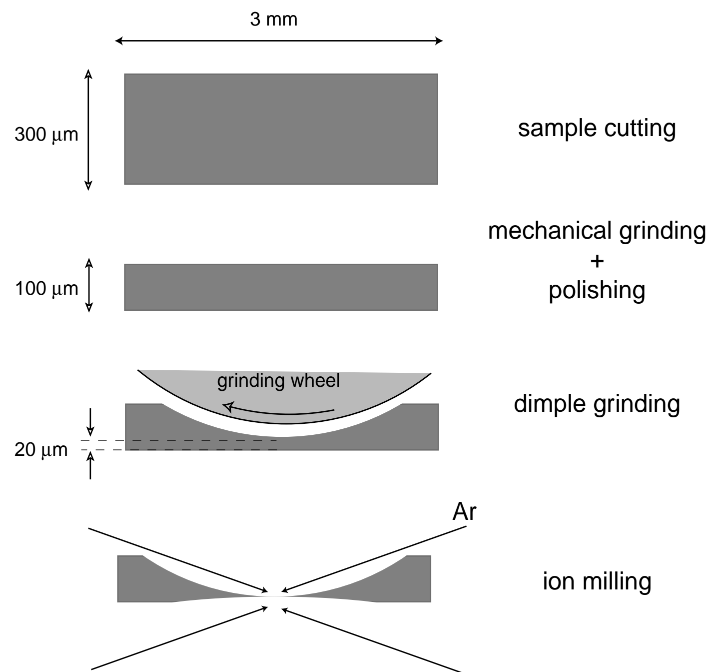

Fig. 3.2 TEM sample preparation of AMCs.

preparation of AMCs due to the low reactivity of the reinforcements in comparison to the unreinforced Al alloys. For AMCs, the following mechanical method was used: TEM foil specimens were prepared by *mechanical dimpling* down to 20 µm, followed by argon ion milling (Fig. 3.2) on a Gatan Duo-Mill machine, operating at an accelerating voltage of 5 kV and 10° incidence angle, with a liquid nitrogen cooling stage to avoid sample heating and microstructural changes associated with the annealing effect. Such effects have been experienced on first samples prepared on an ion mill without cooling stage (PIPS), resulting in an unexpected and substantial coarsening of the precipitation state.

Another preparation method called *focus ion beam* FIB has been tried. A thin slice of the sample was cut by an ion beam on a scanning ion microscope. Unfortunately, the large thickness of the sample (> 150 nm) impeded good HREM studies. The small observable area (100 nm x 100 nm) permitted to study only one or two grains, which is generally not enough if a special grain orientation is required.

3.3 Chemical Analyses by EDS

The first step in phase identification before the analysis of the diffraction patterns is a chemical analysis that can been done in a TEM microscope by *X-rays energy dispersive spectrometry* EDS, or *electron energy loss spectrometry* EELS. In addition to many other advantages such as the possibility of obtaining information on the chemical bonding and its

good spatial resolution, EELS is particularly appropriated for light elements ($Z < Z_{Al}$), but the identification of the chemical elements and the interpretation of the spectra are not as straightforward as in EDS which remains a quick method for identifying and quantifying the elements thanks to user-friendly software. In this work, EDS has been widely used for the identification and, to a lesser degree, for quantification. Basic knowledge of EDS theory is required to be aware about the limitation and the resolution of this technique [43, 44, 45, 46].

The X-ray microanalyses date from 1950's with the thesis of R. Castaing who built a microprobe on a wave dispersive spectrometre (WDS). This was followed in 1956 by the work of Cosslet and Duncumb who developed it on a scanning electron microscope SEM. EDS is now quasi-systematically associated with TEM to constitute a powerful set called *analytical electron microscopy* AEM [47].

Inelastic interactions between electrons and matter give different kinds of signals: secondary electrons, Auger electrons, X-rays, light and lattice vibrations (Fig. 3.1). The X-ray energy corresponds to a difference between two energy levels of the electron cloud of an atom (K, L.). Since these levels are quantified, the X-ray energy spectrum represents the signature of the atom (Fig. 3.3*a*). The X-rays are detected by a semi-conductor and processed by a detector protected by a ultrathin window (Fig. 3.3*b*) and cooled at liquid nitrogen temperature to avoid the thermal noise and the diffusion of the dopant in the semi-conductor. An EDS spectrum is constituted by a background produced by the Bremsstrahlung X-rays and by peaks characteristic to the chemical elements of the material, as shown in Fig. 4.4*c*.

The identification is quite straightforward for elements beyond C when the peaks do not overlap. For lighter elements, the energy of relaxation of excited atoms is in great part carried off as the kinetics energy of Auger electrons (94% of the relaxation process). Moreover, the potential emitted X-rays are in great part absorbed by the window. If there is an overlapping of the peaks, a deconvolution is required, and gives poor results for close elements, such as Mg

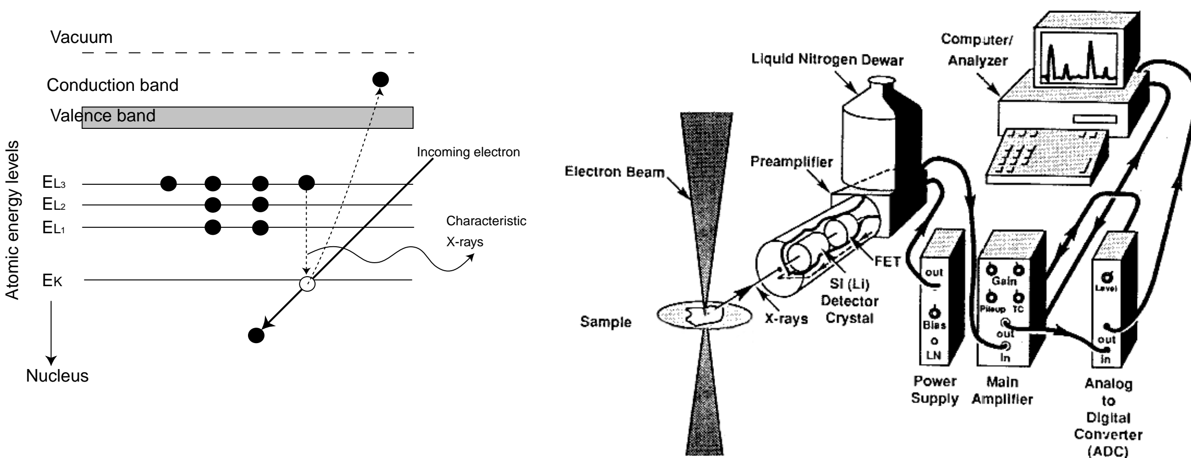

Fig. 3.3 (a) Electronic shell of an atom. The X-rays are emitted by a decrease of one electron from one level to another one, their energies are therefore quantified. (b) X-rays detector in a TEM (modified from [46]).

in an Al matrix. That is the reason why no quantitative results were reported on the Mg content inside the Al matrix of the studied composites. The quantification is more difficult. It takes into account the link between the weight fraction and the generated intensities (ionization cross section) and between the generated intensity and the measured intensity (absorption and fluorescence effects). The measured intensity of an element depends on the other elements present in the sample. For thin samples, where fluorescence and electron absorption are negligible, the weight fraction of the elements are linked by

$$\frac{W_J}{W_A} = k_{JA}\left(\frac{I_J}{I_A}\right)_m \tag{3.2}$$

where W is the weight fraction, I_m the measured intensity and the subscripts represent the element. k_{JA} are the *Cliff-Lorimer ratios*. They can be measured with thin standard specimens of known composition (Cliff-Lorimer method) or calculated for each pair of elements if their ionic cross-sections, fluorescence yields and the detector efficiencies are known (*standardless method*). Then, the ratios are used for other samples containing the corresponding elements. The Cliff-Lorimer method is the most precise one but it imposes a heavy task before obtaining the first results. In this work all the quantifications were done with the standardless method. The thickness of the sample was not taken into account in most of our quantifications on the elements Al, Mg, Si, Cu, Ag because Al, Mg, and Si are very close elements and because the Cu or Ag contents are very low (which reduces the eventual absorption by these elements of X-rays produced by the light atoms). In other cases, for example for the quantification of O, absorption is evaluated after estimating the sample thickness with the thickness fringes observed by TEM in two beam conditions. A precision of 10% can be expected in the quantification (1% with the Cliff-Lorimer method), and of 0.1% for detection threshold in the absence of overlaps. The spatial resolution directly corresponds to the probe size (10 nm for the CM20 microscope and 1 nm for the HF2000 microscope) thanks to the thinness of the TEM samples.

3.4 Electron Scattering: From Diffusion to Diffraction

3.4.1 Diffusion

The electrons are quantum relativistic particles, by consequence their behavior is described by the Dirac equation which time independent Schr dinger equation of classic quantum mechanic (with relativist corrections in the mass of the electron) constitutes a good approximation [48]. Neglecting the interactions between the electrons, the equation for an electron before its interaction with the crystal is

$$\nabla^2\Psi(\boldsymbol{r}) + 4\pi^2 k^2\Psi(\boldsymbol{r}) = 0 \tag{3.3}$$

where $\Psi(r)$ is the wave function associated to the electron and $\boldsymbol{k}$ the wave vector of the electron which is linked to the tension of acceleration U by $k = |\boldsymbol{k}| = \sqrt{2meU}/h$, where m is the relativist mass of the electron given by $m = m_0 (1-\beta^2)^{-1/2}$ where $\beta = v/c$, and e is the absolute value of its charge.
The solution of equation (3.3) is the plane wave function (non-localization plane of the electron) given by $\Psi^{(0)}(\boldsymbol{r}) = \exp[-2\pi i(\boldsymbol{k}^{(0)} \bullet \boldsymbol{r})]$.

During the interaction of the electron with the crystal, the equation is

$$\nabla^2\Psi(\boldsymbol{r}) + \frac{8\pi^2 me}{h^2}[U + V(\boldsymbol{r})]\Psi(\boldsymbol{r}) = 0 \tag{3.4}$$

where $V(\boldsymbol{r})$ is the potential of the crystal. This differential equation can be expressed by an integral form in all the volume of the crystal with the help of the Green function $G(\boldsymbol{r}, \boldsymbol{r}') = \frac{\exp[-2\pi ik(\boldsymbol{r} - \boldsymbol{r}')]}{4\pi|\boldsymbol{r} - \boldsymbol{r}'|}$. It is called the *diffusion equation:*

$$\Psi(\boldsymbol{r}) = \exp[-2\pi i(\boldsymbol{k}^{(0)} \bullet \boldsymbol{r})] + \frac{8\pi^2 me}{h^2}\int_{\Omega} V(\boldsymbol{r}')\Psi(\boldsymbol{r}')\frac{\exp[-2\pi ik|\boldsymbol{r} - \boldsymbol{r}'|]}{4\pi|\boldsymbol{r} - \boldsymbol{r}'|}dv' \tag{3.5}$$

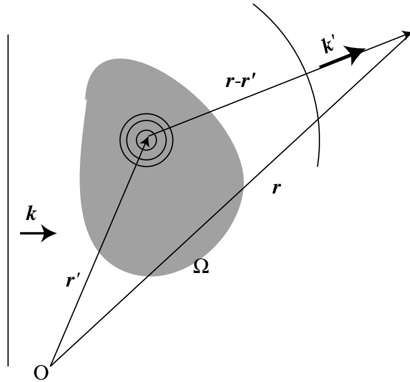

Fig. 3.4 Scattering of an electronic plane wave.

where **k** is vector respecting $|\mathbf{k}| = |\boldsymbol{k}^{(0)}|$. With this equation, one can see that the crystal potential in $\boldsymbol{r}'$ makes diffuse the electron wave in the **k** direction by the intermediate of a spherical wave and a transmission factor given by $(2\pi me/h^2)V(\boldsymbol{r}')$ (Fig. 3.4). This is closely akin to the optical Huygens approach and its general Kirchhoff's formulation [49]. This equation can be solved with some approximations on the form of the electron wave function under the integral (Born approximations). Details are given in [49, 50, 51].

In all the following work, the problem is simplified with the *first Born approximation*, which supposes that the electrons do not interact or interact only one time with the sample. This condition is obtained for a weak $V(\boldsymbol{r})$ and a thin sample; this constitute the *kinematical condition*. The wave function can be written as $\Psi(\boldsymbol{r}) = \Psi^{(0)}(\boldsymbol{r}) + \Psi^{(1)}(\boldsymbol{r})$, with $|\Psi^{(1)}| \ll |\Psi^{(0)}|$. We can therefore replace $|\Psi(\boldsymbol{r}')|$ by $|\Psi^{(0)}(\boldsymbol{r}')|$ in the integral. Assuming that $|\boldsymbol{r}| >> |\boldsymbol{r}'|$, it follows that $|\boldsymbol{r}-\boldsymbol{r}'| = \boldsymbol{r}-(\boldsymbol{r}' \bullet \boldsymbol{k})/k$. Equation (3.5) can be written

$$\Psi^{(1)}(\boldsymbol{r}) = \frac{2\pi me}{h^2}\frac{\exp[2\pi i\boldsymbol{k} \bullet \boldsymbol{r}]}{r}\int_{\Omega} V(\boldsymbol{r}')\exp[2\pi i\boldsymbol{u} \bullet \boldsymbol{r}']dv' \tag{3.6}$$

where $\boldsymbol{u} = \boldsymbol{k}^{(0)}-\boldsymbol{k}$. This expression is very close to that deduced from the general Kirchhoff formula in the *Fraunhofer diffraction* conditions [49]. The integration is done on the volume Ω where the potential is significant; by default the infinity must be taken. It follows that the

amplitude of the scattered wave is

$$A(\boldsymbol{u}) = K\int_{\Omega} V(\boldsymbol{r})\exp[2\pi i\boldsymbol{u} \bullet \boldsymbol{r}]dv \tag{3.7}$$

where $K = 2\pi me/h^2$. The scattered wave function has the form of a Fourier transform integral of the crystal potential. If we neglect the effects of interatomic binding and interactions of atoms on the diffraction intensities, the total potential corresponds to the sum of the contributions of individual atoms a centered at the positions $\boldsymbol{r}_a$:

$$V(\boldsymbol{r}) = \sum_a V_a(\boldsymbol{r} - \boldsymbol{r}_a) \tag{3.8}$$

where V_a is the potential of each individual atom. Equation (3.7) can be written (the atoms being ordered or disordered)

$$A(\boldsymbol{u}) = K\int\sum_a V_a(\boldsymbol{r}' - \boldsymbol{r}_a)\exp[2\pi i\boldsymbol{u} \bullet \boldsymbol{r}']dv' \tag{3.9}$$

or, by exchanging the sum and the integral:

$$A(\boldsymbol{u}) = \sum_a f_a^B(\boldsymbol{u})\exp[2\pi i\boldsymbol{u} \bullet \boldsymbol{r}_a] \tag{3.10}$$

where $f_a^B(\boldsymbol{u})$ is the *atomic diffusion factor* of the atom a given by

$$f_a^B(\boldsymbol{u}) = K\int V_a(\boldsymbol{r})\exp[2\pi i\boldsymbol{u} \bullet \boldsymbol{r}]dv \tag{3.11}$$

By these two equations, it appears that each atom acts as a diffusion center of spherical waves whose amplitudes are given by the atomic diffusion factor with a phase shift of $2\pi\boldsymbol{u} \bullet \boldsymbol{r}_a$. The atomic diffusion factor is proportional to the electron diffusion factor defined by

$$f_a^e(\boldsymbol{u}) = \int V_a(\boldsymbol{r})\exp[2\pi i\boldsymbol{u} \bullet \boldsymbol{r}]dv \tag{3.12}$$

This one is similar to the X-ray diffusion factor (the atomic potential is substituted by the electronic density), even if the interaction processes are different. Both are linked by the Mott formula deduced from the Poisson equation. In general, the atomic diffusion factors are calculated with equation (3.12) as done by Doyle and Turner, the atomic potential being estimated by relativist Hartree-Fock calculi [52, 53]. The very good comparison for Fe, Cu, Al between the calculated and experimental diffusion factors (better than 1% [54]) confirms the validity of equation (3.8). Analytical expressions are given for the diffusion factors in literature [55, 56]. Surprisingly, such analytical expressions do not exist for the radial atomic potential. Therefore, equation (3.12) has been inverted to obtain them. The calculus details are reported in annex A. We found

$$V(r) = -\frac{1}{2\pi r}\frac{d}{dr}\tilde{f}^e(r) \tag{3.13}$$

This formula is used to calculate the radial potential from the analytical expression given by Doyle and Turner of the fitted diffusion factors. Annex A shows that if the diffusion factors are fitted by a sum of Gauss functions, the radial and projected potential is also a sum of Gauss functions. The knowledge of an analytical expression of the radial potentials was used to draw images of disordered materials (section 5.5.3).

3.4.2 Kinematical Diffraction

From equation (3.7), it can be noticed that the amplitude of the diffused spherical wave is proportional to the Fourier Transform ($\Im$) of the atomic potential of the sample, which is the sum of each atomic potential a situated in $\boldsymbol{r}_a$. This Fourier Transform can be directly calculated by the Fast Fourier Transform algorithms (FFT) as illustrated with a finite size crystal in Fig. 3.5. The advantage of the FFT is that the amplitude can be calculated even for non-crystalline particles.

Under the conditions of equation (3.7), the appearance of spots in the diffraction pattern comes from the order that can exist in the sample (crystal, quasicrystal, or other type of order). Crystals are characterized by a translational periodic order (base of the crystallography). This crystal potential can be written

$$V_{cryst}(\boldsymbol{r}) = [V_a(\boldsymbol{r}) \otimes L(\boldsymbol{r})] \cdot E(\boldsymbol{r}) \tag{3.14}$$

where $V_a(\boldsymbol{r})$ is the atomic potential, $L(\boldsymbol{r})$ the periodic lattice of the crystal and $E(\boldsymbol{r})$ the envelope function corresponding to the crystal size. Thus, the amplitude of the diffracted wave (3.7) is proportional to

$$A_{cryst}(\boldsymbol{u}) \propto \tilde{V}_{cryst}(\boldsymbol{u}) = [\tilde{V}_a(\boldsymbol{u})\tilde{L}(\boldsymbol{u})] \otimes \tilde{E}(\boldsymbol{u}) \tag{3.15}$$

For a better illustration, let us reduce the problem to 1 dimensional crystal on size l and assume a Gaussian shape of the potential. The envelope function is then a slit function, where slit $(x, l) = 1$ for $|x| < l/2$ and 0 for $|x| > l/2$. Under these conditions, we have

$$V(x) = \exp[-(x/v)^2] \Rightarrow \tilde{V}_a(u) = \sqrt{\pi} v \exp[-(uv)^2] \tag{3.16}$$

$$L(x) = \sum_{n=-\infty}^{\infty} \delta(x - na) \Rightarrow \tilde{L}(u) = \sum_{n=-\infty}^{\infty} \delta(x - n/a) \tag{3.17}$$

$$E(x) = \mathrm{slit}(x, l) \Rightarrow \tilde{E}(u) = \frac{\sin \pi l u}{\pi u} \tag{3.18}$$

This explains the shape of diffraction profiles, as illustrated in Fig. 3.5. The periodicity of the scattering pattern (diffraction) in $1/a$ comes from the periodicity of the lattice a. This corresponds to the *Laue condition* $\boldsymbol{u} = \boldsymbol{k}^{(0)} - \boldsymbol{k} = \boldsymbol{G}$ detailed in section 3.4.3. The enlargement in $1/l$ of the diffracted peaks comes from the crystal size l. For example, this effect produces the

streaks observed in the electron diffraction patterns acquired on the small θ' plates edge-on (Fig. 4.10*c,d* and Fig. 4.12*a*). The decrease of the peak intensity in u is of the order of $1/v$, it comes from the potential shape v. The broadening of the atomic potential can come from thermal vibrations of the atoms or from a mean disorder of the atoms around their lattice positions (due to random vacancies for instance). The scattering is therefore constituted by the Bragg peaks and two contributions significant for $u << 1/a$ (crystal size effect) and $u >> 1/a$ (thermal vibration). Diffuse peaks can appear for u of the order of $1/a$, it reflects the appearance of superordering in the crystal. This point is treated in section 5.5.

For perfect parallelepiped-shaped crystals, another way to write the amplitude of the diffracted wave can be obtained from equation (3.10) by separating the sum on the lattice (with the volume limitation of the sample) and then on the unit cell:

$$A_{cryst}(\boldsymbol{u}) = \sum_{lattice}\left[\sum_{cell} f_a^B(\boldsymbol{u})\exp[2\pi i\boldsymbol{u}\bullet\boldsymbol{r}_a]\right]\exp[2\pi i\boldsymbol{u}\bullet\boldsymbol{r}_l]$$

$$= F^B(\boldsymbol{u})\cdot G^B(\boldsymbol{u}) \tag{3.19}$$

where $F^B(\boldsymbol{u}) = \sum_{cell} f_a^B(\boldsymbol{u})\exp[2\pi i\boldsymbol{u}\bullet\boldsymbol{r}_a]$ (3.20)

and $G^B(\boldsymbol{u}) = \sum_{cell}\exp[2\pi i\boldsymbol{u}\bullet\boldsymbol{r}_l]$ where $\left|G^B(\boldsymbol{u})\right| = \frac{\sin\pi hlN_x}{\sin\pi h}\frac{\sin\pi kN_y}{\sin\pi k}\frac{\sin\pi lN_z}{\sin\pi l}$ (3.21)

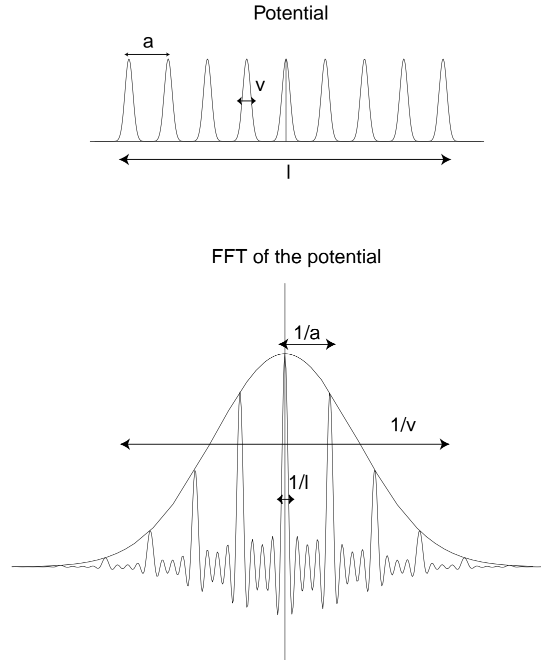

Fig. 3.5 One dimensional view of (a) the potential of a crystal and (b) its Fourier Transform (proportional to the amplitude of the diffused wave)

where $\boldsymbol{u} = (h, k, l)$ and N_x, N_y, N_z are the numbers of unit cells constituting the lattice in the x, y, z directions. $F^B(\boldsymbol{u})$ is defined as the *structure factor*, it corresponds to the diffusion factor of the unit cell and includes de atom vibrations (3.16) by the intermediate of the atomic diffusion factor (3.11), and $G^B(\boldsymbol{u})$ is defined as the *shape factor*, it includes the lattice (3.17) and its envelope (3.18).

3.4.3 Bragg Law

Another way to describe diffraction is to notice that it occurs when the waves diffused by any cell separated by a vector of the lattice $\boldsymbol{r}$ are in coherence, i.e. when the phase shift is $2\pi.n$ where n is a relative integer. This is written by $\boldsymbol{u} \cdot \boldsymbol{r} = n$ where $\boldsymbol{u} = \boldsymbol{k}^{(0)} - \boldsymbol{k}$. This condition is equivalent to impose that $\boldsymbol{u}$ is vector of the reciprocal space. This is the *Laue law*:

$$\boldsymbol{u} = \boldsymbol{G} \qquad (3.22)$$

Noting θ_B, the semi-angle between $\boldsymbol{k}^{(0)}$ and $\boldsymbol{k}$, by geometrical considerations, we can notice that $/\boldsymbol{u}| = 2\sin\theta_B/\lambda$, where λ is the wavelength of the electrons. Moreover, one property of the reciprocal vector is $|\boldsymbol{G}| = 1/d_{(h,k,l)}$ where $d_{(h,k,l)}$ is the interplanar spacing of the diffracting planes. Therefore, the Laue law $/\boldsymbol{u}| = |\boldsymbol{G}|$ gives the *Bragg law*:

$$2d_{(h,k,l)}\sin\theta_B = n\lambda \qquad (3.23)$$

3.4.4 Ewald Construction

As illustrated in Fig. 3.5, it can be noticed that the Laue condition $\boldsymbol{u} = \boldsymbol{k}^{(0)} - \boldsymbol{k} = \boldsymbol{G}$ at the origin of the Bragg peaks is not completely required to obtain an intensity in the SAED pattern: the size effect of the sample or of the observed particle allows a tolerance around the Bragg peaks written by $\boldsymbol{u} = \boldsymbol{k}^{(0)} - \boldsymbol{k} = \boldsymbol{G} + \boldsymbol{s}_h$, where $\boldsymbol{s}_h$ is called *excitation error vector*. The diffraction condition can be reported using the Ewald sphere as illustrated in Fig. 3.6. The diffraction pattern appears to be the intersection between the Ewald sphere and the reciprocal lattice of the crystal convoluted with the shape factor. A symmetric pattern corresponds to large $\boldsymbol{s}_h$ at large $\boldsymbol{G}$ vectors (called *Laue condition*) as in Fig. 3.6; a two beam condition corresponds to $\boldsymbol{s}_h = 0$ (called *Bragg condition*). The *zero order Laue zone* (ZOLZ) pattern corresponds to the intersection of the Ewald sphere with the vectors $\boldsymbol{u}$ of the reciprocal space normal to a direction of the direct space $\boldsymbol{r}$ called a *zone axis*: $\boldsymbol{u} \cdot \boldsymbol{r} = 0$. The *high order Laue zones* (HOLZ) patterns of index n correspond to the intersection of the Ewald sphere with the vectors $\boldsymbol{u}$ of the reciprocal space linked to the zone axis by the Laue law: $\boldsymbol{u} \cdot \boldsymbol{r} = n$. A small convergence of the electron beam permits a loss of localization of the Ewald sphere which tilts around the $\boldsymbol{G} = (000)$ point, and favors the appearance of the spots on the diffraction pattern. This is useful for the observations of the HOLZ.

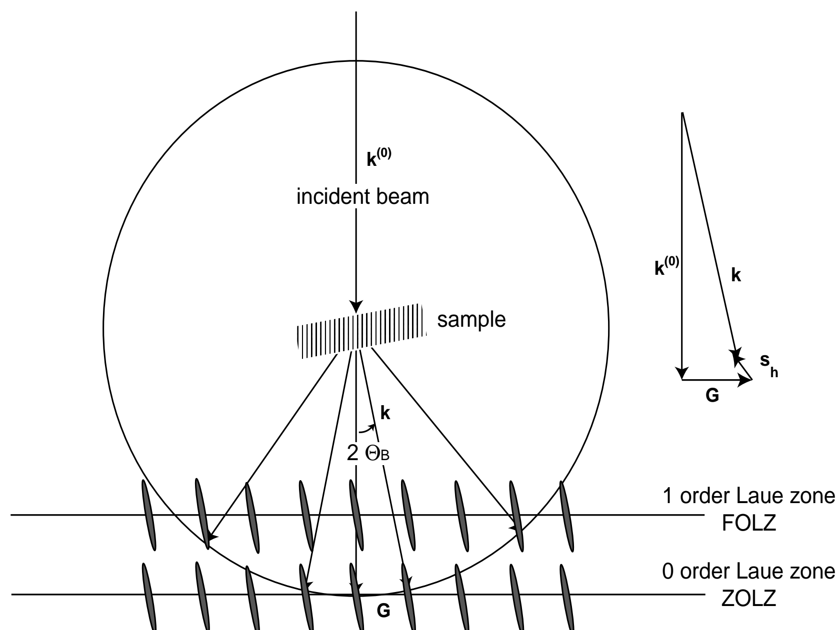

Fig. 3.6 Diffraction conditions $\boldsymbol{u} = \boldsymbol{k}^{(0)} - \boldsymbol{k} = \boldsymbol{G} + \boldsymbol{s}_h$ *reported on the Ewald sphere* $|\boldsymbol{k}^{(0)}|=|\boldsymbol{k}|$. *Only the ZOLZ planes are represented. The spikes associated to the reciprocal space come from the sample size effect.*

3.4.5 Dynamical Diffraction

In the previous part, the electron diffraction has been introduced with the first Born approximation (kinematical diffraction). For strong potentials, for large sample thickness (in comparison with a distance called the extinction distance), or when there are few diffracted beams with low $|\boldsymbol{s}_h|$ values, the intensity of the diffracted beams is not negligible in comparison to the transmitted beam, and the approximation is no longer valid. The transmitted and diffracted wave functions follow then a system of linear equations called the *Howie-Whelan equations*. They correspond to the coupling between the transmitted and diffracted beams. Details are given in [49, 50, 51].

3.5 Conventional Transmission Electron Microscopy

3.5.1 Imaging Mode

A transmission electron microscope is constituted of: (1) two or three condenser lenses to focus the electron beam on the sample, (2) an objective lens to form the diffraction in the back focal plane and the image of the sample in the image plane, (3) some intermediate lenses to magnify the image or the diffraction pattern on the screen. If the sample is thin (< 200 nm) and constituted of light chemical elements, the image presents a very low contrast when it is

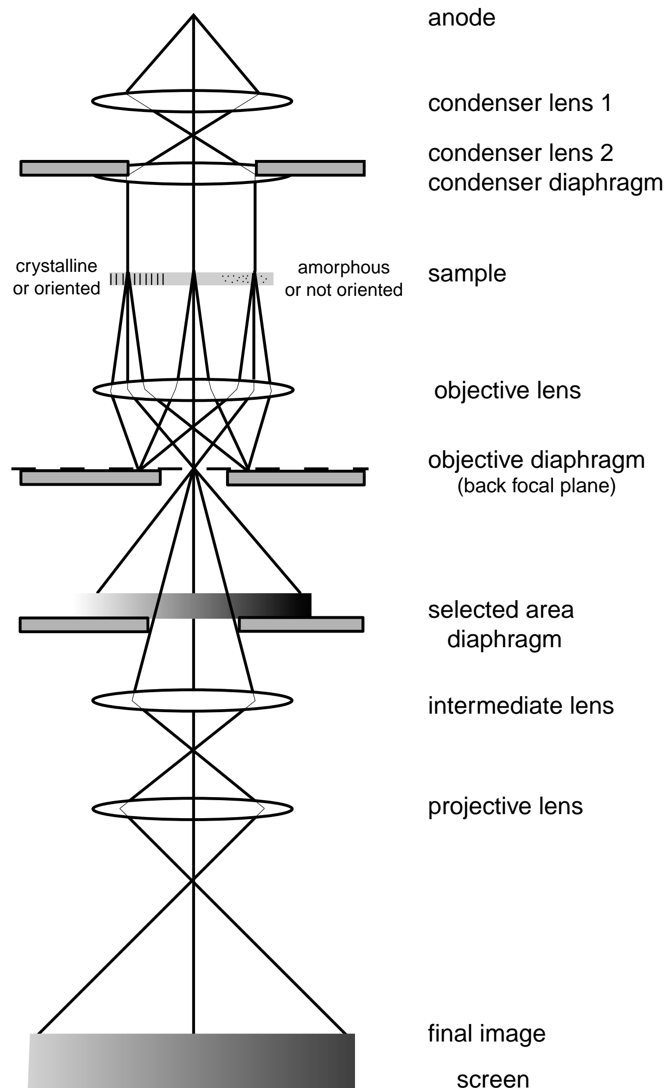

Fig. 3.7 Ray diagram for a transmission electron microscope in image mode. In diffraction mode, an other intermediate lens is inserted to image on the screen the diffraction pattern of the back focal plane.

focused. To obtain an amplitude contrasted image, an objective diaphragm is inserted in the back focal plane to select the transmitted beam (and possibly few diffracted beam): the crystalline parts in Bragg orientation appear dark and the amorphous or not Bragg oriented parts appear bright. This imaging mode is called *bright field* mode BF (Fig. 3.7). If the diffraction is constituted by many diffracting phases, each of them can be differentiated by selecting one of its diffracted beams with the objective diaphragm. To do that, the incident beam must be tilted so that the diffracted beam is put on the objective lens axis to avoid off-axis aberrations (Fig. 3.8). This mode is called *dark field* mode DF. The BF and DF modes are used for imaging materials to nanometer scale.

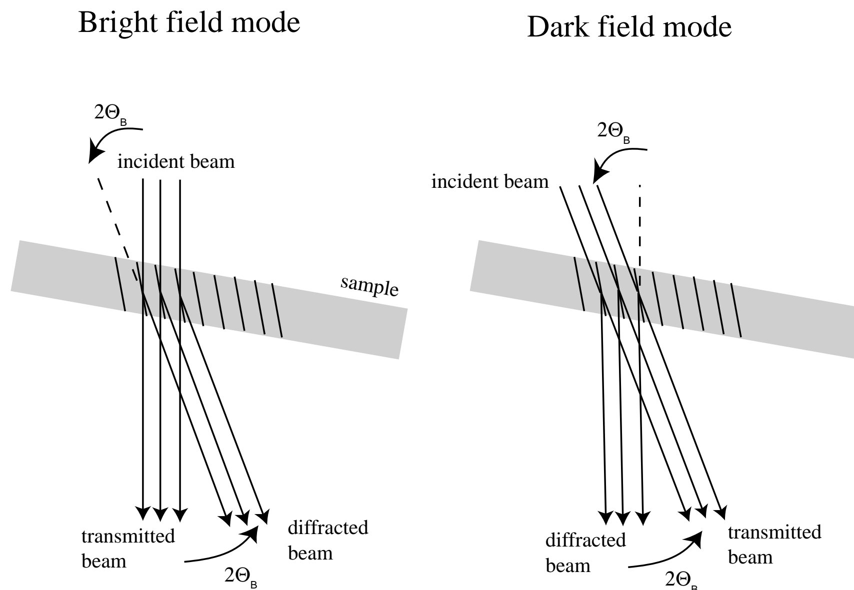

Fig. 3.8 Bright and dark field modes for imaging.

3.5.2 Diffraction Mode

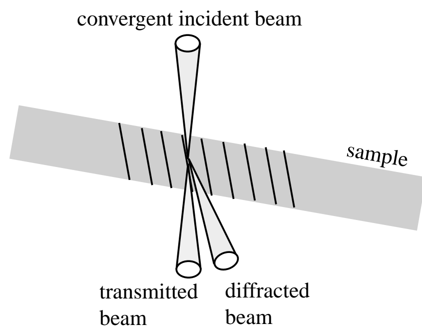

Fig. 3.9 Microdiffraction mode

The selected area diaphragm is used to select only one part of the imaged sample for example a particle or a precipitate. This mode is called *selected area diffraction* SAED. The spherical aberrations of the objective lens limit the area of the selected object to few hundred nanometers. Nevertheless, it is possible to obtain diffraction patterns of a smaller object by focusing the electron beam with the projector lenses to obtain a small spot size on the object surface (2-10 nm). The spots of SAED become disks whose radii depend on the condenser diaphragm. This is called *microdiffraction* (Fig. 3.9).

SAED and microdiffraction patterns of a crystal permit to obtain the symmetry of its lattice and calculate its interplanar distances (with the Bragg law (3.23)). This is useful to confirm the identification of a phase, after assumptions generally based on the literature of the studied system and on chemical analyses (see section 3.3).

These techniques were applied to identify the interfacial reaction products, intermetallic phases and fine precipitation in the AMCs (chapter 4).

3.5.3 Special TEM Techniques

Microdiffraction and Convergent Beam Electron Diffraction CBED

As seen in the previous section, focusing the incident beam favors the acquirement of the HOLZ in the diffraction patterns. The whole pattern WP (ZOLZ + HOLZ patterns) and the bright field pattern BF (deficient HOLZ lines in the 000 disk) bring 3-D information on the observed crystal.

Microdiffraction gives the symmetry of the WP, this allows the determination of the Laue class and in consequence of the crystal system (see annex C.1). Moreover, the possible shift between the ZOLZ and the FOLZ patterns is connected with the Bravais modes, the possible periodicity difference between the ZOLZ and the FOLZ pattern is connected with the presence of glide planes. These pieces of information are a first step to the space group determination. Details are given in [57]. The advantage of this method is that it has few limitations, it allows the study of small particles [58], and the possibility of observing small areas allows quantitative measurements without any thickness or orientational variations.

CBED is more informative than microdiffraction. It uses the symmetry of the WP but also the details inside the diffraction disks in dynamical conditions to break the Friedel's law. The determination of the point group is based on the symmetry of the dynamical HOLZ lines[1] present in the transmitted beam and in the diffracted beam, and on the symmetry between +g/ -g beams. Details are given in [59, 60]. In addition, the determination of the space group stands on the Gj¿nnes and Moodie lines[2] to assess all the helical axes or glide planes.

Some aspects of microdiffraction and CBED were used for the determination of some polytypic structures of the SiC particles (Fig. 4.8*a*). A quantitative study based on the intensity of ZOLZ disks obtained by microdiffraction were performed to determine the atomic positions in the precipitates present in the AlCuMgSi and AlMgSi alloys (Fig. 6.12).

Scanning Transmission Electron Microscopy STEM

The basic principle of image formation in the STEM is fundamentally different from static beam TEM: a small spot size is formed on the sample surface with the condenser lenses. This probe is scanned on the sample surface with scan coils, and in parallel, the signal is detected by an electron detector, amplified and synchronously displayed on a cathode-ray tube (CRT) with the scan coils. The detector can be a small disk on the column axis which detects only the transmitted beam (BF STEM image) or a diffracted beam (DF STEM image), or can

1. The HOLZ lines are observed as dark lines in the transmitted beam. They come from a deficit of electron due to an elastic scattering with the HOLZ planes (a bright line is observed in their corresponding spots). The HOLZ lines can be observed outside the transmitted beam when the electron beam has been inelastically scattered before the elastic collision. They are called Kikuchi HOLZ lines.
2. The Gj¿nnes and Moodie lines appear as dark lines in disks lighten in dynamical condition but which should have been extinguished in kinematical condition. They come from the presence of helicoidal axes or glide planes [61].

be an annular detector (a plate with a hole) which detects all the diffracted beams except the transmitted one (ADF STEM). The resolution of the image is only limited by the spot size (quality of the condenser lenses) since the objective lens is not used. In general, STEM images have poorer resolution but better contrast than TEM images. ADF STEM with high angle (>50 mrad) can be used to make chemical images[1], but in general the contrast in ADF STEM images is determined by the diffraction. This technique was used for the observation of the fine Si precipitates in the matrix of a WFA/Al_2O_3 composite (Fig. 4.16*a*).

3.6 High Resolution Transmission Microscopy

Conventional TEM uses only the transmitted beams *or* some of the forward scattered beams to create a diffraction contrast image. HREM uses the transmitted *and* the scattered beams to create an interference image. As it will be detailed in the following parts, the TEM microscope must have a high performance (low spherical aberrations and high stability of the high tension, of the lens currents and of the energy of the electron beam). The understanding of the image formation must take into account the two following steps: (1) the propagation of the incident wave through the object, (2) the transfer of the scattered wave by an optical system of the microscope (the objective lens).

3.6.1 Propagation through the sample

The propagation of the incident wave through the sample is usually treated with one of these two different methods: the Bloch waves method or the *multislice method*. Both are applicable to perfect crystals, but in addition the multislice method is also applicable to crystals with defects or to non-periodic structures. It is based on the physical optics approach given by Cowley and Moodie [62]. A complete description is given in [50, 51, 63].

The crystal of total thickness z is cut into many slices of small thickness Δz. The difference between the wave vector in vacuum $k_v = \sqrt{2meU}/h$ and the one in each slice $k_m = \sqrt{2me(U+V(r))}/h$ creates a refraction index given by

$$n_r = (k_m/k_v) = \sqrt{(U+V(r))/U} \cong 1 + V(r)/2U \tag{3.24}$$

which introduces a phase shift between the transmitted and the scattered wave

$$d\alpha = (\boldsymbol{k}_m - \boldsymbol{k}_v) \bullet d\boldsymbol{r} = (n_r - 1)k_v dz = \frac{k_v}{2U}V(\boldsymbol{r})dz \tag{3.25}$$

1. Annular detectors with large holes called high angle ADF detectors can be used to detect the diffused electrons (the incoherence of high angle scattered electrons make the diffraction impossible) and form images with a signal proportional to the diffusion factor and therefore linked to the mass. These images are called *Z-contrast images*. They can reach atomic level resolution on the best TEM with FEG guns.

Therefore, for each slice, the phase shift is given by

$$\Delta\alpha_n = \frac{k_v}{2U}\int_{z_n}^{z_n+\Delta z} V(x,y,z)dz = \frac{k_v}{2U}V_p(x,y,z_n) \tag{3.26}$$

where $V_p(x, y, z_n)$ is the projected potential of the nth slice. When the wave Ψ_n comes through the nth slice, the phase shift can be expressed by multiplying the wave function by a function called the *transmittance function* given by

$$q_n(x,y) = \exp[-2\pi i\Delta\alpha_n] = \exp[-i\sigma V_p(x,y,z_n)] \tag{3.27}$$

where $\sigma = (\pi k_v)/U = \pi/(\lambda U)$ is the relativistic interaction constant.

Then, we can consider that the wave propagates on a distance Δz. The propagation of a wave near an object follows the Fresnel approximation: the wave is convoluted with the Fresnel propagator:

$$p_{n\to n+1}(x,y) = \frac{\exp[-2\pi i\Delta z]}{i\lambda\Delta z}\exp\left[-\frac{i\pi}{\lambda\Delta z}(x^2+y^2)\right] \tag{3.28}$$

In consequence, the multislice interaction cycle can be written

$$\Psi_{n+1} = (\Psi_n \bullet q_n) \otimes p_{n\to n+1} \tag{3.29}$$

which permits to calculate the wave after its propagation through the sample, called the *exit wave function* Ψ_e.

For a thin area constituted of light atoms, the exit wave function is given directly by equation (3.27) (only half an iteration), which can be developed to the first order:

$$\Psi_e(x,y) \cong 1 - i\sigma V_p(x,y) \tag{3.30}$$

This approximation is called *weak phase object* approximation. In this equation, the unity corresponds to the transmitted beam and the other term to the scattered beam. Since the diffracted beam is out of phase by $\pi/2$ with the transmitted one, it cannot interfere with the transmitted beam! Fortunately, as shown in the following section, the objective lens of the microscope additionally introduces another phase shift which makes the interference possible. Since the mean projected potential is about 200 V.Å for an Al atom (see annex A), σV_p is about 0.1 and the weak phase object approximation is restricted to one or two Al monolayers.

3.6.2 Transfer by the optical system

As usual in transfer theory, the wave transferred through the optical system (the image

wave) is the convolution between the object wave (exit wave) and a *transfer function* $T(\boldsymbol{r})$:

$$\Psi_i(\boldsymbol{r}) = \Psi_e(\boldsymbol{r}) \otimes T(\boldsymbol{r}) \tag{3.31}$$

which is equivalent to

$$\tilde{\Psi}_i(\boldsymbol{u}) = \tilde{\Psi}_e(\boldsymbol{u}) \bullet \tilde{T}(\boldsymbol{u}) \tag{3.32}$$

In coherent illumination, and without astigmatism, the transfer function T is given by

$$\tilde{T}(\boldsymbol{u}) = a(\boldsymbol{u})\exp 2\pi i\chi(\boldsymbol{u}) \tag{3.33}$$

where

$$\chi(\boldsymbol{u}) = \frac{1}{4}C_s\lambda\boldsymbol{u}^4 + \frac{1}{2}\Delta f\lambda\boldsymbol{u}^2 \tag{3.34}$$

where $a(\boldsymbol{u})$ represents an optional diaphragm of size d in the back focal plane of the objective lens ($a(\boldsymbol{u}) = 1$ for $|\boldsymbol{u}| < \mathrm{d}$ and 0 for $|\boldsymbol{u}| > \mathrm{d}$), C_s is the spherical aberration coefficient of the objective lens and Δf a defocus value. In fact, the fluctuations of the incident electron energy, of the acceleration voltage and of the objective lens current added to an possible convergent beam effect, damp the CTF for the high spatial frequencies. All the terms of equation (3.34) can be written as envelope functions which limit the information of the HREM images.

In the case of a weak phase object, the image wave deduced by equations (3.30) and (3.31) is

$$\Psi_i(x, y) = [1 - i\sigma V_p(x, y)] \otimes T(x, y) = 1 + \sigma V_p \otimes \mathrm{Re}T - i\sigma V_p \otimes \mathrm{Im}T \tag{3.35}$$

Since $\sigma V_p \ll 1$, the image intensity is given by

$$I(x, y) = |\Psi_i|^2 = 1 + 2\sigma V_p \otimes \mathrm{Im}T \tag{3.36}$$

Therefore, in the weak phase object approximation, only the imaginary part of the transfer function ImT contributes to the intensity of the image by transmitting the phase information (the amplitude information, negligible for weak phase object, is transferred by ReT). ImT is represented in Fig. 3.10 with two different defocus values.

Resolution and interpretation

As shown in Fig. 3.10, ImT is an oscillating function whose shape depends on the defocus value. Each zero implies a loss of the phase information at the corresponding frequency. The "best" transfer function is the one close to 1 for the larger frequency scale. Scherzer has shown [64] that it can be obtained for a particular defocus value:

$$\Delta f_{Sch} = -\sqrt{\frac{4}{3}C_s\lambda} \tag{3.37}$$

At Scherzer defocus Im$T(\boldsymbol{u}) \approx$ -1 in a large range of $\boldsymbol{u}$, therefore Im$T(x,y) \approx \delta_{x,y}$ and equation

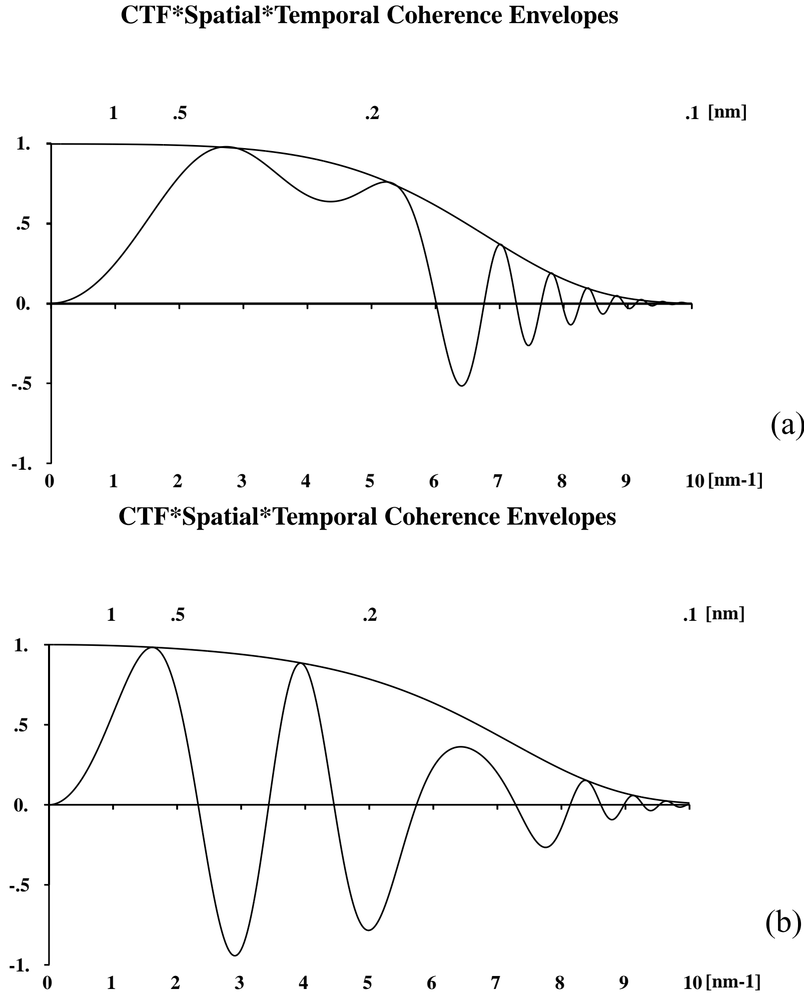

Fig. 3.10 Negative imaginary part of the effective transfer function $\tilde{T}(\boldsymbol{u})$ *of the CM300UT-FEG microscope with their spatial and temporal damping envelopes at (a)* Δf *= -48 nm Scherzer defocus and (b)* Δf *= -100 nm*

(3.36) gives

$$I(x,y) = 1 - 2\sigma V_p(x,y) \tag{3.38}$$

Under these conditions, the image is a direct representation of the projected atomic potential. Nevertheless, at Scherzer defocus $\mathrm{Im}T(\boldsymbol{u}) \approx -1$ is valid only for frequencies smaller than the first zero of $\mathrm{Im}T(\boldsymbol{u})$ noted h_{Sch}. This frequency defines the *point resolution* ρ of the microscope (also called Scherzer resolution):

$$h_{Sch} = 1.51 C_s^{-1/4} \lambda^{-3/4} \tag{3.39}$$

$$\rho = 1/h_{Sch} = 0.66 C_s^{1/4} \lambda^{3/4} \tag{3.40}$$

In fact, as shown in Fig. 3.10, information is transmitted at higher frequencies, but due to the oscillations, this information cannot be directly interpreted and simulations are required. The transmission is yet limited by the envelope damping functions and imposes an *information limit*.

3.7 Quantitative Electron Crystallography

3.7.1 Phase Loss Problem in Diffraction

All the information concerning the nature and the positions of the atoms is given by $A(\boldsymbol{u})$ (3.7) or, for crystalline materials, by the structure factor $F^B(\boldsymbol{u})$ (3.20). For a unit-cell constituted by many atoms, the atomic positions are in great part given by the phases of the structure factor [65, 66]. The diffraction intensities give only $|F^B(\boldsymbol{u})|^2$ and the phases are lost. This is the well-known phase problem of X-ray crystallography. Even if in general the number of relationships given by the link between $F^B(\boldsymbol{u})$ and the acquired intensities greatly exceeds the number of unknown atomic positions, no analytical solution exists. The only information on the direct space is given by the inverse Fourier Transform of $A(\boldsymbol{u})$:

$$P(\boldsymbol{r}) = \Im^{-1}(|A(\boldsymbol{u})|^2) = V(\boldsymbol{r}) \otimes V(-\boldsymbol{r}) = \int V(\boldsymbol{r})V(\boldsymbol{r}+\boldsymbol{R})d\boldsymbol{R} \tag{3.41}$$

where *P(r)* is the *Patterson function*, which corresponds to the spatial autocorrelation function of the atomic potential. This formula is for example used in X-ray crystallography (replace the atomic potential by the electronic density) in the so-called *heavy atom method*.

Direct methods are also possible and effective thanks to the very good precision in the X-ray intensity measurements on large monocrystals [67]. These methods try to derive the structure factor phases directly from the obtained amplitude through mathematical relationships (Sayre’s equations). However, these methods cannot be performed with electron diffraction due to the low precision in the intensities and some potential dynamical effects. The situation is changing with new CCD cameras and imaging plates, even if the curvature of the Ewald sphere remains a problem for the high spatial frequencies. Moreover, electron microscopists are more interested in mixed structures or small particles which are very difficult to study by X-rays.

3.7.2 HREM “Direct” Methods

The direct interpretation of an HREM image is only possible on very thin samples (weak phase object) at Scherzer defocus. In general, these conditions are not fulfilled and the problem remains unsolved: “what is the structure?”. Some position parameters of a previous physical structural model can be refined by exploiting the CBED intensities [68]. However, in total absence of any previous physical model, some authors have worked to exploit the HREM images as much as possible to elaborate this crystal model that is further refined using the

diffraction intensities. Indeed, although HREM images contain some phase information characteristic of the atomic positions, the resolution obtained is low due to the CTF functions; on the other hand, diffraction patterns contain information up to higher frequencies due to the absence of any CTF, but only in modulus form. The use of HREM images and/or electron diffraction patterns for structure determination is called *electron crystallography* [69]. This technique dates from the 1950's [70] but has not been widely used until the two last decades due to the complexity of the dynamical effects. Actually, electron crystallography is a complementary technique of X-ray crystallography: the strong interaction between electron and matter (thousands of times stronger than X-rays) enables the structural determination of crystals of a few nanometers size with, in some cases, precisions on the atomic positions comparable to those obtained with X-rays (~ 0.02 Å). Two electron crystallography techniques based on HREM images have recently emerged:

(1) the reconstruction of the exit wave by acquiring HREM images at different defocus values named *through focus exit wave reconstruction* (TF-EWR) [71, 72]. The resulting structure is refined with the diffraction intensities recorded on a CCD camera, with a software which includes the excitation error and the dynamical effects, called *multi-slice least squares* (MSLS) [73]. The atomic position precision is ~ 0.2 Å. This method has several drawbacks such as the necessity to know exactly the defocus steps and the heavy task to treat 20 HREM images. Moreover, one fundamental difficulty (but very shortly treated by the authors) is the passage from the exit wave function to the determination of the chemical element and its real position. For example, the structure of the β'' phase in the AlMgSi alloys was claimed to be successfully determined [74] with excellent reliability factors. The determination was, however, based on a composition Mg_5Si_6 determined by chemical X-ray analysis performed on the precipitate embedded in the Al matrix whereas recent X-rays studies on β'' precipitates extracted from the Al matrix reveals the presence of Al (30%-at) [75, annex B2].

(2) the processing of HREM images of thin samples by *crystallographic image processing* (CRISP) [76]. This permits to extract the phase and the amplitudes of the HREM image and correct them by considering the changes introduced by the transfer function, the astigmatism (and possibly the tilt). The second step imposes to this corrected image the "most probable" symmetry (determined by minimizing the sum on each reflection of the phase differences between the image and the "symmetrized" image in which the phases of some reflection are linked by the symmetry). The structure is then refined with the SAED intensities, using a computer program which uses the X-ray refinement methods with the electron diffusion factors. A precision close to the X-rays one (~ 0.02 Å) is obtained [77]. The drawback of the method is the need for very thin samples, so as to be as close as possible to the weak phase object approximation. Moreover, large objects are required to evaluate correctly the validity of the symmetrization since the method relies in great part on the hypothesis of the periodicity of the crystal. Therefore, this method is not well adapted to observations of defects or disorder, but remains a high-performance, crystallographic "filtering" process.

3.7.3 HREM Simulations

Once a structural model is proposed for a crystal, its validity should be checked by HREM image simulations, at least when the sample is not a weak phase object. However, this is rarely done by the users of direct HREM methods. The HREM simulations must take into account the crystal parameters (the model structure to be checked, with the Debye-Waller factors and its structure factor), its thickness, and some TEM parameters such as C_s, Δf, the crystal tilt, the accelerating voltage, the beam divergence and the astigmatism. Simulation programs are available [78].

In this work, the crystallographic structure of the β' phase has been determined (see section 6.3) by the refinement of the atomic positions given by a previous model with the intensities of microdiffraction patterns. HREM simulations were performed to check the refined structure. The two "direct" methods could not be applied due to their major drawbacks.

3.8 TEM Facilities

All the TEM observations have been done at the Interdepartmental Center of Electron Microscopy (CIME, EPFL). Most of the chemical analyses, and all the SAED and microdiffraction patterns and superstructure images were performed on a conventional Philips CM20T-LaB_6 TEM microscope operating at 200 kV and equipped with a EDS Noran Voyager. DSTEM images, some EDS measurements on small rod-shaped precipitates, and HREM images have been performed on an Hitachi HF2000-FEG TEM microscope operating at 200kV. Most of the HREM images have been obtained with a Philips CM300UT-FEG TEM operation at 300kV. All HREM images were acquired on a CCD camera using the Gatan Digital Micrograph software. Their eventual processing has been done with this software. TEM in-situ heating experiments were performed on the CM20 microscope using a Gatan double tilt heating holder. The parameters of the microscopes are presented in Table 3.1.

	Philips CM20T-LaB_6	Hitachi HF2000-FEG	Philips CM300UT-FEG
E_0 [kV]	200	200	300
C_s [mm]	2.0	1.2	0.6
ρ [nm]	0.28	0.23	0.17
s [nm]	10	5	6
α [mrad]	1	0.25	0.25
d [nm]	10	1.5	2.2

Table 3.1 Parameters of the TEM microscopes used in this work. E_0 accelerating voltage, C_s spherical aberration coefficient, ρ point resolution, s focus spread, α semi-angle of convergence, d smallest probe size.